Chinese Chemical Letters 36 (2025) 110309

Contents lists available at ScienceDirect

Chinese Chemical Letters

journal homepage: www.elsevier.com/locate/cclet

Synergistic effects of oxygen vacancies and Pd single atoms on Pd@TiO_{2-x} for efficient HER catalysis

Xiaoyu Zhao[a], Kai Gao[a], Sen Xue[a], Wei Ran[b], Rui Liu[b,c,*]

[a] Tianjin Key Laboratory of Brine Chemical Engineering and Resource Eco-utilization, College of Chemical Engineering and Materials Science, Tianjin University of Science and Technology, Tianjin 300457, China
[b] State Key Laboratory of Environmental Chemistry and Ecotoxicology, Research Center for Eco-Environmental Sciences, Chinese Academy of Sciences, Beijing 100085, China
[c] School of Environment, Hangzhou Institute for Advanced Study, UCAS, Hangzhou 310024, China

ARTICLE INFO

Article history:
Received 19 February 2024
Revised 25 June 2024
Accepted 30 July 2024
Available online 31 July 2024

Keywords:
Electrocatalytic water splitting
Single-atom Pd catalysts
Oxygen vacancies
Synergistic effects
HER catalysis

ABSTRACT

Electrocatalytic water splitting for hydrogen production is a key approach to tackling the current energy crisis. Among the catalysts, the traditional Pd@C catalysts are remarkable for their efficiency in hydrogen evolution. However, the high cost and scarcity of Pd catalysts, as well as the instability caused by the corrosiveness of carbon-based substrates, hinder their large-scale application. To overcome this challenge, an effective strategy is to construct highly dispersed Pd single atoms to improve palladium utilization and choose more stable materials as supports. In this study, TiO_{2-x} carriers with abundant oxygen vacancies were prepared and loaded with Pd by photoreduction deposition. Adjusting the palladium content resulted in three forms of Pd-loaded TiO_{2-x}: nanoparticles (Pd@TiO_{2-x}(6%, 10%)), nanoclusters (Pd@TiO_{2-x}(3%)) and single atoms (Pd@TiO_{2-x}(1.5%)). The oxygen vacancies improved the stability of the titanium dioxide materials by providing more active hydrogen adsorption sites and increasing the affinity of Pd for active hydrogen. Single atom loading increased the frequency of oxygen holes in the support and the high activity of monatomic Pd promoted the adsorption of active hydrogen and facilitated the formation of active hydrogen intermediates. The synergistic effect of single atoms and oxygen vacancies improved the stability and catalytic activity of the composite material. Pd@TiO_{2-x}(1.5%) showed outstanding performance in hydrogen evolution in an acidic medium with an overpotential of only 24 mV at a current density of 10 mA/cm^2 and a low Tafel rise of 41.9 mV/dec. This study provides an effective strategy for the development of high-performance hydrogen evolution (HER) catalysts .

The widespread use of fossil fuels has led to severe energy consumption and environmental pollution [1,2]. Hydrogen energy, due to its high energy density, low cost, lack of pollution, and zero carbon emissions, is considered the most promising clean energy source [3]. Electrochemical water splitting driven by renewable electricity is an ideal and efficient hydrogen production technology. However, the sluggish kinetics of the hydrogen evolution reaction (HER) at the cathode significantly hinders large-scale hydrogen production [4-6]. To enhance the kinetics of the HER, reduce the reaction overpotential, and design efficient and durable HER electrocatalysts is crucial. Currently, Pt@C and Pd@C catalysts are the most efficient commercial hydrogen evolution electrocatalysts [7]. However, their high cost and material instability, prone to deactivation due to corrosion during usage, hinder their widespread application. Therefore, there is an urgent need to explore more economically efficient electrocatalysts [8-10].

Considerable efforts have been devoted to developing novel precious metal HER electrocatalysts (*e.g.*, Ru, Rh, Pt, and Ir) [11-13]. Among them, Pd is considered one of the most promising candidate materials [14]. Numerous Pd-based catalyst materials have been applied to electrocatalytic hydrogen evolution. Heydari-Bafrooei *et al.* synthesized a Pd/WS_2 catalyst with inorganic fullerene WS_2-supported Pd nanoparticles using a sol-gel immobilization method [15]. By encapsulating Pd nanoparticles within WS_2 cages for the HER reaction, the catalyst material's activity was improved, demonstrating excellent long-term stability [16]. Liu *et al.* through electrodeposition, anchored Pd nanoparticles onto MoS_x/TiO_2 nanotube arrays, enhancing the carrier's electrical conductivity [17]. The introduction of Pd nanoparticles significantly improved the carrier's conductivity, and the electronic

* Corresponding author.
E-mail address: ruiliu@rcees.ac.cn (R. Liu).

https://doi.org/10.1016/j.cclet.2024.110309
1001-8417/

structure of MoS_x weakened the Pd-H bond, promoting hydrogen desorption and enhancing electrocatalytic activity [18]. Zheng *et al.* used a highly conductive MOF as a template to prepare a Pd@MOF-74-M composite catalyst [19]. The small size and high dispersion of Pd nanoclusters, as well as the effective protection provided by the MOF framework, exhibited excellent HER catalytic activity [20]. Gao *et al.* successfully synthesized sub-nanometer Pd clusters in porous cerium dioxide (Pd NCs@CeO_2) [21]. The electron transfer between Pd and O atoms in the material effectively regulated the adsorption state of active hydrogen on Pd clusters, promoting the HER catalytic activity of the composite system [22]. To further reduce the cost of precious metals and maximize atomic utilization, single-atom catalysis has garnered significant attention [23]. Single-atom catalysts (SACs), composed of single metal atoms fixed on carrier materials, can maximize the exposure of active sites, improve atomic utilization, reaction selectivity, and enhance the system's electrocatalytic activity [24]. Yu *et al.* reported graphene (GDY)-supported zero-valent Pd atoms on ultrathin nanosheets for direct application as a three-dimensional flexible hydrogen evolution cathode [25]. The successful anchoring of individual dispersed palladium atoms on GDY maximized the atomic efficiency and the number of active sites, greatly improving catalytic activity. Zhu *et al.* anchored isolated Pd atoms on $Ti_3C_2T_x$ MXene, optimizing hydrogen adsorption on MXene and effectively enhancing water molecule dissociation through strong electronic interactions between MXene layers, improving HER activity [26]. However, the low electrical conductivity, low loading density, and poor stability and tolerance of single-atom catalysts severely limit their application and catalytic efficiency [27]. Therefore, selecting a suitable stable material as a precious metal carrier is necessary.

To enhance the catalytic performance, stability, and selectivity of precious metals, researchers have developed various carriers, such as metal oxides, metal nitrides, metal phosphides, and metal sulfides [28-32]. For example, Wang *et al.* coated ruthenium with ruthenium oxide on TiO_2, demonstrating excellent stability for hydrogen electro-oxidation [33]. Zeng *et al.* reported a highly efficient nano-composite electrocatalyst composed of Pd NPs uniformly embedded in mesoporous oxygen-deficient TiO_2 nanospheres [34]. Doping Ti^{4+} sites induced the formation of abundant oxygen vacancies in mesoporous TiO_2 nanospheres, enhancing the activity and stability of the composite material. Due to its richness and good physicochemical properties, titanium dioxide has been widely studied as a substrate for depositing precious metals to enhance catalytic performance and stability [35]. Compared to TiO_2, TiO_{2-x} with abundant oxygen vacancies has received more attention due to its superior conductivity, catalytic activity, and stronger stability [36,37]. Zhang *et al.* reported that TiO_{2-x} substrates not only stabilized MoS_2 but also promoted the adsorption and dissociation of water molecules during the HER process [38]. The composite material MoS_2/TiO_{2-x}@Ti exhibited excellent catalytic performance. Additionally, Zhang *et al.* designed a structure decorating TiO_{2-x} nanotube arrays with CoP_3/CoMoP nanosheets [39]. The oxygen vacancy-rich TiO_{2-x} nanotube structure provided more active sites, enhancing HER performance. Wu *et al.* developed a one-step rapid method without the need for high temperature and inert gas protection to synthesize oxygen-deficient black TiO_2-supported sub-nanometer Pt clusters with metal-support interactions [40]. The metal-support interactions between Pt and black TiO_2 endowed the prepared composite material with excellent electrocatalytic performance for HER [41]. The coupling effect between oxygen vacancies and Pt optimized the electron density around Pt, thereby optimizing the adsorption free energy of hydrogen and improving the electrocatalytic performance of HER in acidic media [42]. Moreover, the strong interaction between Pt and oxygen-deficient titanium dioxide significantly enhanced the stability of the designed electrocatalyst [43].

In this study, TiO_2(B) was selected as the precursor material. Through annealing in an argon atmosphere, it was transformed into oxygen-deficient TiO_{2-x} as the carrier. Using a photoreduction deposition method, Pd single atoms were successfully anchored on the surface of oxygen-deficient titanium dioxide. The newly synthesized Pd@TiO_{2-x}(1.5%) composite material (TiO_{2-x} material with Pd content of 1.5%) exhibited significantly superior HER activity. Benefiting from the ultra-stable oxygen-deficient titanium dioxide carrier, the composite material demonstrated robust long-term electrocatalytic stability, with almost no decline in activity after 1000 cycles. Further density functional theory (DFT) theoretical calculations indicated that the presence of oxygen vacancies improved the stability and catalytic activity of the material, promoting the generation of more active sites and enhancing the adsorption of active hydrogen by precious metal Pd. Additionally, by adjusting the Pd loading amount, Pd-loaded TiO_{2-x} materials of different morphologies were prepared. The presence of single-atom Pd significantly increased the abundance of oxygen vacancies, and Pd, as the main active center, greatly promoted the generation of active hydrogen intermediates, reducing the Gibbs free energy of hydrogen and accelerating the electrocatalytic kinetics of HER. The synergistic effect of single atoms and oxygen vacancies collectively promoted the high catalytic activity and stability of the composite material.

Transmission electron microscopy (TEM), and elemental mapping analysis were performed using a Philips Tecnai F30 at 300 kV. Powder X-ray diffraction (XRD) was performed on Panalytical X′pert PRO X-ray diffractometer with monochromated Cu Kα radiation (40 kV, 30 mA). Inductively coupled plasma atomic mass spectrometry (ICP-MS) measurements were performed on PerkinElmer. X-ray photoelectron spectroscopy (XPS) was carried out on PHI5000VPIII hemispherical electron energy analyzer with monochromatized Al Kα radiation (1486.6 eV). Electron paramagnetic resonance (EPR) was performed at Bruker EMX-10/12 with the temperature at 293 K.

To prepare the catalyst dispersion, Pd@TiO_{2-x} material (10 mg) and XC-72R carbon black (5 mg) were placed in a mixture of isopropanol (0.5 mL) and 5% Nafion (0.05 mL). The mixture was sonicated for 1 h, and then 10 μL of the dispersion was drop-cast onto a glassy carbon electrode, resulting in a loading rate of 0.013 mg Pd/cm^2 for the catalyst. The addition of carbon black to the catalyst dispersion enhances the electronic conductivity of the electrode surface and the dispersibility of the catalyst. The electrode preparation process for other materials was identical, using commercial Pd@C (10%) and Pt@C (10%) as reference materials.

All electrochemical tests were conducted using a three-electrode system on a CHI440C electrochemical workstation, with a Pt mesh (20 × 20 mm) as the counter electrode, Ag/AgCl as the reference electrode, and glassy carbon as the working electrode. All tests were performed in a nitrogen-saturated 0.5 mol/L H_2SO_4 solution. Potentials were referenced to the reversible hydrogen electrode (RHE), and the results were calculated using Eq. 1.

$$E_{RHE} = E_{Ag/AgCl} + 0.059pH + 0.237 \quad (1)$$

Linear sweep voltammetry (LSV) was performed at a scan rate of 5 mV/s after 30 cyclic voltammetry (CV) cycles of preconditioning. Tafel slope was determined from the LSV curve. Catalyst stability was assessed by performing 1000 CV cycles (100 mV/s). Chronoamperometry was conducted by recording the time-current density curve at 10 mA/cm^2. Double-layer capacitance (C_{dl}) was determined from CV curves at various scan rates (20, 40, 60, 80, 100 mV/s) within a specific potential window.

DFT was employed as implemented in the Vienna *Ab initio* simulation package (VASP) for all calculations. The exchange-correlation potential was described using the generalized gradient approximation of Perdew-Burke-Ernzerhof (GGA-PBE). The pro-

jector augmented-wave (PAW) method was utilized to treat interactions between ion cores and valence electrons. The plane-wave cutoff energy was fixed at 500 eV [44]. The structural models were relaxed until the Hellmann-Feynman forces were smaller than −0.02 eV/Å and the change in energy was smaller than 10^{-5} eV.

During the relaxation, the Brillouin zone was represented by a Γ centered k-point grid of $6 \times 6 \times 1$ [45]. Grimme's DFT-D3 methodology was employed to describe the dispersion interactions among all the atoms in the adsorption models.

According to XRD analysis, the main component of TiO_{2-x} is rutile, thus the model structure of rutile is used as the carrier structure [46]. The TiO_2 (101) surface was modeled using two three-layer periodic slabs. The lattice constants for the (3×2) TiO_2 (101) unit cell were set as follows: $a = 11.05$ Å, $b = 11.49$ Å, $c = 25.00$ Å. To further investigate the role of oxygen vacancies, a single oxygen was removed from the (3×2) TiO_2 (101) surface, according to reference [47]. Simultaneously, to account for the influence of the surface periodic structure, a vacuum layer was set to 15.00 Å.

Single Pd, optimized Pd13 clusters, and Pd(111) species were adsorbed on the TiO_2 (101) surface with a single oxygen removed, representing single-atom Pd, cluster Pd, and nano Pd, respectively, for the structural optimization of Pd-based catalysts [48]. The optimized configurations were subjected to Bader charge, differential charge, and density of states analyses [49]. Multiple adsorption configurations and positions were considered for all adsorbate species, and the subsequent calculations selected the lowest energy and most stable configurations. The formula for calculating hydrogen adsorption energy (ΔE_H) is as follows:

$$\Delta E_H = E_{M+H} - E_M - \frac{1}{2} E_{H_2} \quad (2)$$

E_{M+H} represents the total energy associated with the absorption of a single hydrogen atom on the surface of Pd@TiO_{2-x} material [50]. E_M denotes the total energy of Pd@TiO_{2-x}, and E_{H_2} signifies the energy of a gaseous hydrogen molecule (approximately −6.7 eV in this study) [51]. The Gibbs free energy correction for hydrogen absorption incorporates adjustments for entropy and zero-point energy:

$$\Delta G_H = \Delta E_H + \Delta E_{ZPE} - T\Delta S_H \quad (3)$$

ΔE_H represents the adsorption energy of hydrogen, ΔE_{ZPE} denotes the difference in zero-point energy between the adsorbed state of hydrogen and gaseous hydrogen, and ΔS_H signifies the entropy difference between the adsorbed state of hydrogen and gaseous hydrogen [52]. Since the contribution of vibrational entropy for the adsorbed state of hydrogen is negligible, it can be ignored. The adsorption entropy for hydrogen gas is denoted as $\Delta S_H \approx -\frac{1}{2} S_{H_2}$, where S_{H_2} represents the entropy of the H_2 gaseous phase under standard conditions. Therefore, the corrected Gibbs free energy is expressed as follows:

$$\Delta G_H = \Delta E_H + 0.24 \quad (4)$$

Fig. S1a (Supporting information) illustrates the precursor as the typical TiO_2(B) phase. The Raman spectrum of TiO_2(B), depicted in Fig. S1b (Supporting information), reveals Raman vibrational peaks at 256, 382, 422, 477, 553, 632 and 828 cm^{-1}. These peaks confirm that the prepared precursor material is purely TiO_2(B). Fig. 1a presents the XRD patterns of Pd-loaded TiO_{2-x} with different proportions. Two peaks at 25.3° and 48.0° are attributed to the (101) and (200) crystal planes of anatase, respectively, and two peaks at 27.4° and 36.1° are assigned to the (110) and (101) crystal planes of rutile (JCPDS, 99-0008 and 99-0090, respectively) [53]. It can be inferred that, under argon atmosphere, after calcination at 800 °C for 3 h, TiO_2(B) transforms into anatase and rutile phases, indicating a structural change. No distinct Pd characteristic diffraction peaks are observed in the XRD patterns of Pd@TiO_{2-x}(1.5%) and Pd@TiO_{2-x}(3%), attributed to the small size and good dispersion of single-atom Pd and Pd clusters, making them undetectable by XRD. In the XRD patterns of Pd@TiO_{2-x}(6%) and Microscopy (TEM). The morphology of TiO_2, as shown in Fig. S2 (Supporting information), appears as a two-dimensional (2D) nanosheet. The morphology of TiO_{2-x}, as shown in Fig. 1b, is closer to a particulate form. Figs. 1c and d are TEM images of TiO_{2-x} further magnified after increasing the resolution, where lattice fringes with spacings of 0.351 nm and 0.324 nm are measured [54]. These spacings correspond to the (101) lattice plane of the TiO_2 anatase phase and the (110) lattice plane of the rutile phase, respectively, consistent with the XRD results mentioned earlier. The morphology of Pd@TiO_{2-x}(1.5%) and Pd@TiO_{2-x}(3%) is shown in Figs. 1e and f, where no obvious Pd aggregation is observed, and there are no distinct Pd lattice fringes. This is attributed to the low Pd loading in the 1.5% material, and the extremely small size of Pd single atoms, making them challenging to observe clearly by TEM. As shown in Fig. 1f, Pd@TiO_{2-x}(3%) predominantly exhibits Pd clusters in an entirely exposed form. This confirms the successful anchoring of Pd clusters on the TiO_{2-x} material. The morphology of Pd@TiO_{2-x}(6%) and Pd@TiO_{2-x}(10%) is shown in Figs. 1g and h, indicating uniform distribution of Pd NPs on the carrier. Furthermore, by increasing the resolution and measuring lattice fringe spacings, distinct lattice fringes with a spacing of 0.224 nm corresponding to the (111) crystal plane of Pd NPs are clearly observed. Particle size distribution analysis shows that the nanoparticle size of Pd@TiO_{2-x}(6%) is approximately 5.91 nm, and that of Pd@TiO_{2-x}(10%) is approximately 9.96 nm, as shown in Figs. S3a and b (Supporting information). To verify the existence of single atoms in Pd@TiO_{2-x}(1.5%), aberration-corrected high-angle annular dark-field scanning transmission electron microscopy (AC-HAADF- STEM) was employed for characterization, as illustrated in Fig. 1i. This clearly shows that Pd is predominantly distributed as individual atoms uniformly on the surface of the TiO_{2-x} carrier, confirming the successful preparation of single atoms (Figs. S4a and b in Supporting information).

The near-surface charge states of the catalyst materials were investigated using XPS. Figs. 2a and b present the XPS spectra of TiO_{2-x}, revealing the predominant presence of Ti and O elements of TiO_{2-x}. The Ti 2p peaks of TiO_{2-x} are located at 464.7 eV and 459.0 eV, corresponding to the $2p_{1/2}$ and $2p_{3/2}$ states of Ti^{4+}, respectively. These binding energies are lower than the Ti 2p peaks in pure anatase, which are at 465.5 eV and 459.5 eV, indicating a shift towards lower binding energy possibly due to electron gain from oxygen-deficient atoms in TiO_2. In the O 1s spectrum, the three peaks at 529.7, 532.6, and 533.4 eV correspond to lattice oxygen in O-Ti, oxygen atoms near oxygen vacancies, and surface-adsorbed water molecules, respectively. Notably, the peak at 532.6 eV has a larger area, suggesting a significant presence of oxygen vacancies [55]. This is advantageous for fine-tuning the chemical and electronic structures of the material surface, promoting enhanced reactivity. To further validate the generation of oxygen vacancies, Raman spectroscopy was performed on the materials, as shown in Fig. 2c. The Raman peaks corresponding to the anatase and rutile phases of titanium dioxide were detected in TiO_{2-x}, consistent with XRD results. The peak at 142 cm^{-1} is attributed to the E_g vibrational mode of the anatase phase, the peak at 515 cm^{-1} to the $A_{1g} + B_{1g}$ vibrational mode of the anatase phase, the peak at 448 cm^{-1} to the E_g vibrational mode of the rutile phase, and the peak at 612 cm^{-1} to the A_{1g} vibrational mode of the rutile phase. Anatase phase of titanium dioxide belongs to the tetragonal crystal phase, and in the tetragonal crystal system, changes in the vibrational peak of the E_g mode can serve as direct evidence of oxygen vacancy defect formation. The generation of oxygen vacancies can enhance the sample's conductivity and charge transfer capability [56]. By comparing the most intense vibrational peaks

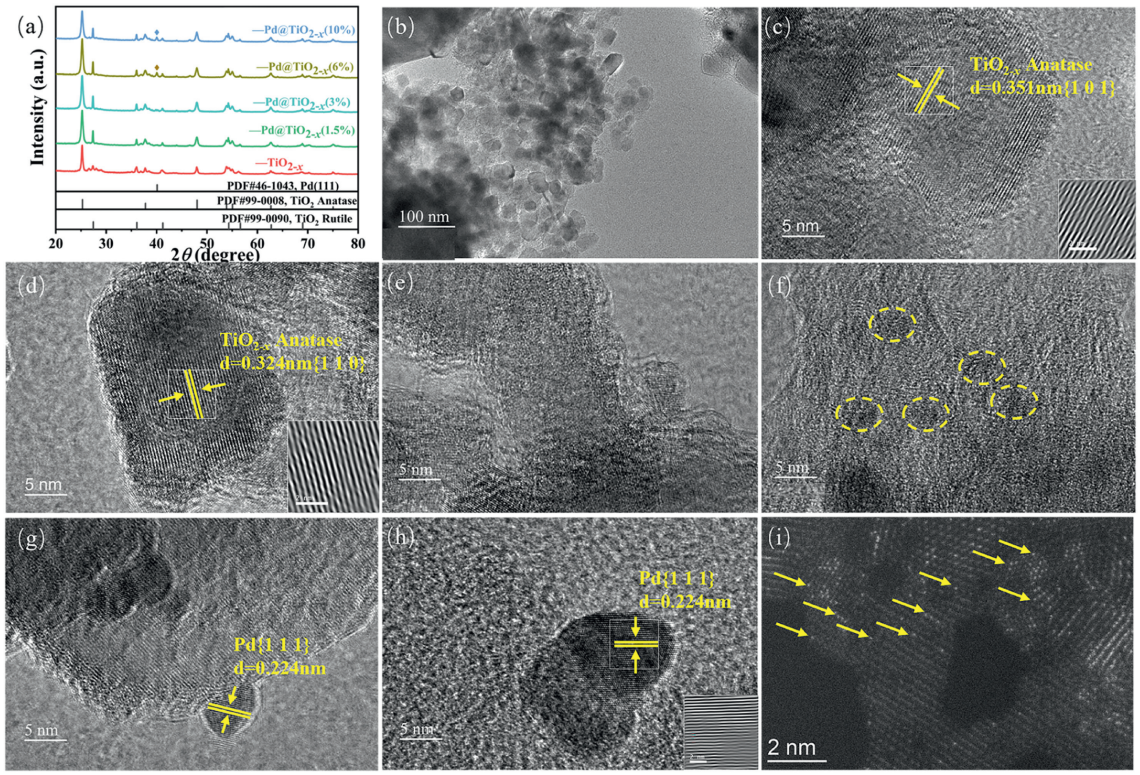

Fig. 1. (a) XRD patterns of TiO_{2-x}, Pd@TiO_{2-x}(1.5%), Pd@TiO_{2-x}(3%), Pd@TiO_{2-x}(6%), Pd@TiO_{2-x}(10%). (b) TEM images of TiO_{2-x}. (c, d) TEM images of different crystal forms of TiO_{2-x}. (e-h) TEM images of Pd@TiO_{2-x}(1.5%), Pd@TiO_{2-x}(3%), Pd@TiO_{2-x}(6%), Pd@TiO_{2-x}(10%). (i) HAADF-STEM image of Pd@TiO_{2-x}(1.5%).

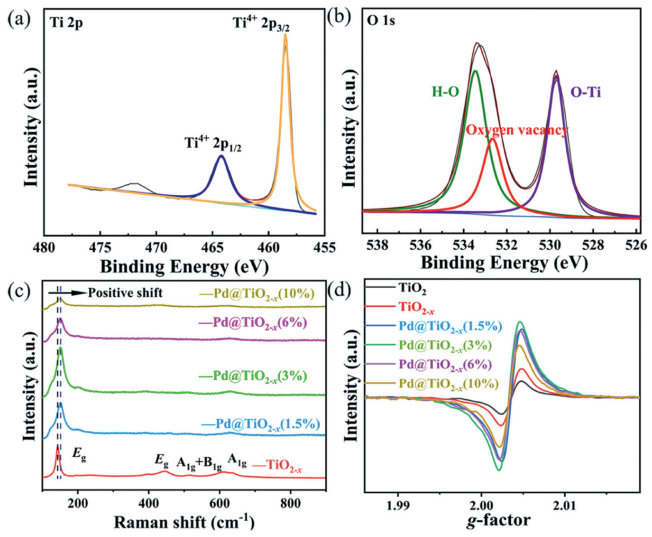

Fig. 2. (a, b) High-resolution XPS Ti 2p and O 1s spectrum of TiO_{2-x}. (c) Raman spectrums of TiO_{2-x}, Pd@TiO_{2-x}(1.5%), Pd@TiO_{2-x}(3%), Pd@TiO_{2-x}(6%), Pd@TiO_{2-x}(10%). (d) EPR spectra of different catalyst.

of the E_g mode for all materials in the anatase phase (~142 cm^{-1}), it is observed that the TiO_{2-x} material is anchored by Pd atoms, lattice defects are induced by the strong Pd-O bonding interaction, resulting in more oxygen vacancies, and the crystallinity of TiO_{2-x} changes, resulting in wider distribution of vibration modes [57,58]. Additionally, electron paramagnetic resonance spectroscopy (EPR) was employed to further confirm the presence of oxygen vacancies in the materials [59]. The results, as shown in Fig. 2d, reveal no apparent EPR peaks in TiO_2, while TiO_{2-x} and Pd@TiO_{2-x}(1.5%) both exhibit a sharp peak at $g = 2.003$, consistent with the characteristic EPR peak of oxygen vacancies [60]. Moreover, at $g = 1.983$, there is no distinct Ti^{3+} peak, indicating that the oxygen vacancies in TiO_{2-x} and Pd@TiO_{2-x}(1.5%) are generated during the crystalline phase transition in a high-temperature argon atmosphere. Similar phenomena have been reported in previous literature. From the spectra, it is evident that the signal peak of oxygen vacancies is significantly enhanced when single-atom Pd is loaded onto the TiO_{2-x} carrier [61]. This enhancement is attributed to the strong interaction between Pd and the TiO_{2-x} carrier after the introduction of single-atom Pd, forming a robust Pd-O bonding, thereby facilitating the generation of oxygen vacancies on the carrier. By comparing the intensities of characteristic peaks, it is inferred that single-atom Pd, when combined with the TiO_2 carrier, provides the maximum abundance of oxygen vacancies [62]. High-resolution X-ray photoelectron spectroscopy was performed on Pd-loaded TiO_{2-x} with different proportions to determine the chemical states of different Pd forms, as shown in Fig. S5 (Supporting information). The Pd $3d_{5/2}$ peaks of Pd@TiO_{2-x}(1.5%) (336.4 eV), Pd@TiO_{2-x}(3%) (336.2 eV), Pd@TiO_{2-x}(6%) (335.4 eV), and Pd@TiO_{2-x}(10%) (335.1 eV) are located between Pd^0 (335.0 eV) and Pd^{2+} (337.9 eV), indicating that Pd is in an oxidized state. With increasing Pd loading, the binding energy of Pd 3d shifts towards lower energy, suggesting a strong interaction between highly dispersed Pd single atoms and clusters with the TiO_{2-x} carrier. The binding energies of Pd@TiO_{2-x}(1.5%) and Pd@TiO_{2-x}(3%) for Pd $3d_{3/2}$ are 341.7 eV and 340.9 eV, respectively. No peaks at 335.0 eV are observed for the single-atom and cluster forms, indicating the absence of distinct Pd-Pd bonds on these two materials [63]. This is consistent with TEM results, confirming the successful anchoring of isolated single atoms and clusters on the TiO_{2-x} carrier. Furthermore, the higher binding energy of single-atom Pd compared to cluster Pd and nano Pd indicates a stronger interaction between single-atom Pd and the TiO_{2-x} carrier.

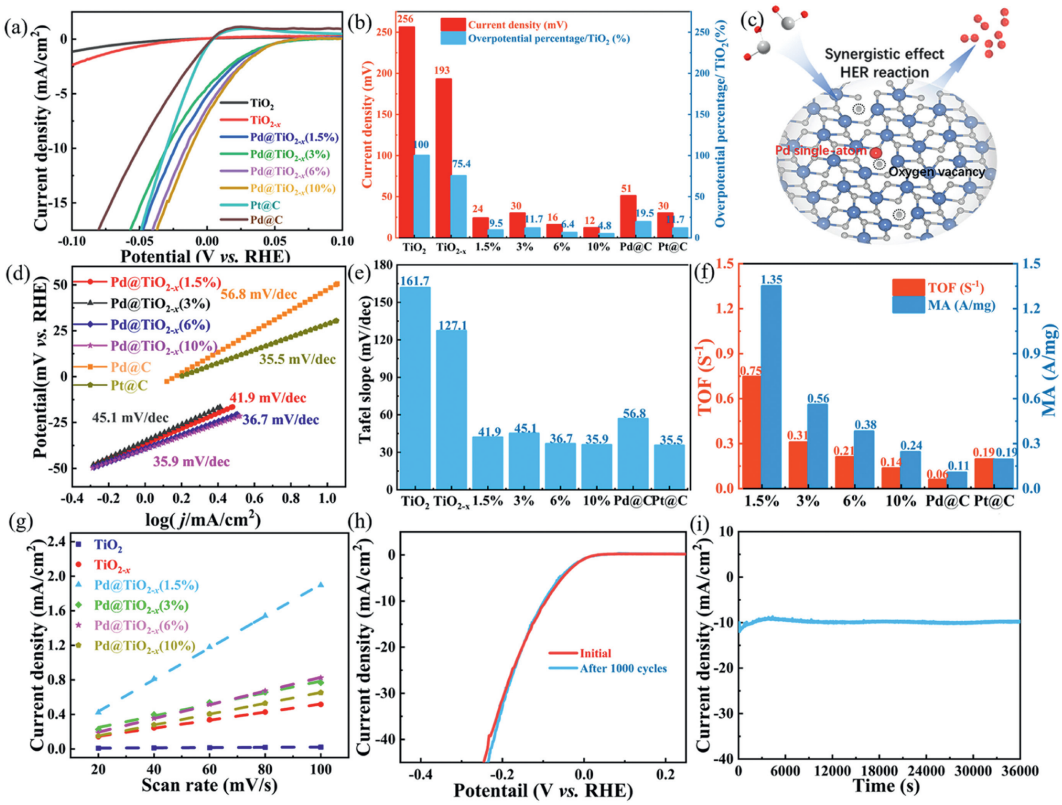

Fig. 3. (a, b) HER polarization curves and overpotential histogram of as-prepared samples in 50 mmol/L H_2SO_4, respectively. (c) Schematic illustration of the HER mechanism on Pd@TiO_{2-x}(1.5%). (d, e) Tafel plots and Slope histogram of prepared samples in 50 mmol/L H_2SO_4, respectively. (f) TOF curves with respect to Pd or Pt atoms and mass activities (based on Pd or Pt mass loading) at $\eta = 50$ mV of catalysts. (g) Corresponding current density scan rate curves to estimate the Cdl, respectively. (h) Cycling stability tests of Pd@TiO_{2-x}(1.5%) by 1000 cycles. (i) Long-term chronoamperometry measurements at a current density of 10 mA/cm^2 of Pd@TiO_{2-x}(1.5%).

The hydrogen evolution reaction (HER) performances of TiO_2, TiO_{2-x}, Pd@TiO_{2-x}(1.5%), Pd@TiO_{2-x}(3%), Pd@TiO_{2-x}(6%), Pd@TiO_{2-x}(10%), Pd@C(10%), and Pt@C(10%) were systematically evaluated in a 0.5 mol/L H_2SO_4 solution saturated with N_2 using steady-state linear sweep voltammetry (LSV). As depicted in Figs. 3a and b, TiO_2 and TiO_{2-x} exhibit large overpotentials of 256.5 mV and 193.5 mV, respectively. The presence of oxygen vacancies reduces the overpotential by approximately 25%, demonstrating that oxygen vacancies on the carrier surface contribute to an enhancement in catalytic activity.

This is attributed to the increased crystallinity and conductivity associated with the introduction of oxygen vacancies, leading to reduced charge transfer resistance and improved catalytic performance. Upon Pd loading onto the surface of TiO_{2-x}, the overpotential decreases by about 90%, confirming that the high HER activity primarily originates from Pd species. Additionally, the overall electrocatalytic performance of Pd@TiO_{2-x} surpasses that of commercial Pt@C (30 mV) and commercial Pd@C (51 mV), exhibiting higher HER activity. Remarkably, Pd@TiO_{2-x}(1.5%) achieves a current density of 10 mA/cm^2 at an overpotential of 24 mV with a low loading rate of 0.013 mg Pd/cm^2. The strong Pd-O bonding interaction between single-atom Pd and the oxygen vacancies, this may be due to the introduction of heavier Pd atoms that affect the coordination structure of TiO_2 [64], on the TiO_{2-x} carrier facilitates the generation of oxygen vacancies, as confirmed by the EPR results [65]. The robust Pd-O interaction and increased oxygen vacancies synergistically contribute to the enhanced catalytic performance, as illustrated in Fig. 3c.

Figs. 3d and e present Tafel test results for different materials. Pure TiO_2 exhibits the highest slope, with a value of 161.72 mV/dec. The presence of oxygen vacancies in TiO_{2-x} enhances the catalytic performance, resulting in a slope of 127.15 mV/dec. Upon loading precious metal Pd onto TiO_{2-x}, the prepared Pd@TiO_{2-x} materials exhibit a significant reduction in Tafel slope. The Tafel slopes for Pd@TiO_{2-x} materials with different Pd contents are 41.9, 45.1, 36.7 and 35.9 mV/dec, indicating that the HER process of Pd@TiO_{2-x} materials follows the Volmer-Heyrovsky mechanism, and materials with loaded Pd metals show faster reaction kinetics.

The intrinsic activity of the catalysts was verified by turnover frequency (TOF), assuming that all Pd sites on the catalyst contacted the electrolyte and participated in the HER process. As shown in Fig. 3f, the TOF values of Pd@TiO_{2-x}(1.5%) are 2.4 times, 3.5 times, 5.6 times, and 12.5 times higher than those of Pd@TiO_{2-x}(3%), Pd@TiO_{2-x}(6%), Pd@TiO_{2-x}(10%), and Pd@C, respectively. When normalized to Pd loading, Pd@TiO_{2-x}(1.5%) exhibits outstanding mass activity (2.63 A/mg) at an overpotential of 0.05 V, surpassing the mass activities of Pd@TiO_{2-x}(3%), Pd@TiO_{2-x}(6%), Pd@TiO_{2-x}(10%), and Pt@C. This indicates that the loading of single-atom Pd substantially enhances the intrinsic activity of each catalytic site on the titanium dioxide surface. Notably, the catalytic activity of Pd single atoms exceeds that of Pd clusters and Pd nanoparticles.

Fig. 3g displays the electrochemically active surface area of the catalyst materials. Pd@TiO_{2-x}(1.5%) exhibits the highest double-layer capacitance value, significantly exceeding those of Pd@TiO_{2-x}(3%), Pd@TiO_{2-x}(6%), and Pd@TiO_{2-x}(10%), indicating that single-atom palladium enlarges the active surface area of TiO_{2-x}. Stability is a crucial factor in evaluating catalysts. Fig. 3h demonstrates that Pd@TiO_{2-x}(1.5%) only attenuates by 1% after 1000 cycle scanning of LSV, maintaining good cyclic performance and verifying its stability in terms of catalytic performance. Furthermore, Fig. 3i shows Pd@TiO_{2-x}(1.5%) at the current density of

10mA/cm^2 was tested by chronopotentiometric method, and it was found that it only decreased by 0.8% after 10 h, which verified its outstanding stability. Fig. S6 (Supporting information) shows Pd@TiO_{2-x}(1.5%) exhibits the smallest semicircle of all the electrocatalysts studied with a charge-transfer resistance of 97.83 Ω (Table S1 in Supporting information), implying the fastest charge transfer rate at the electrode and electrolyte interface.

To further elucidate the impact of differently shaped Pd-loaded oxygen-deficient titanium dioxide on the hydrogen evolution (HER), DFT calculations [66]. Based on the XRD and Raman results, the rutile TiO_2(101) surface was employed as a carrier model, as depicted in Fig. S7 (Supporting information), and constructed oxygen vacancies by removing individual oxygen layer of the TiO_2(101) surface: 2-coordinated bridging O (O_{2c}) and 3-coordinated in-plane O (O_{3c}), as illustrated in Fig. S8 (Supporting information). The optimized energy clearly indicates that removing 2-coordinated bridging O atoms leads to the formation of more stable oxygen-deficient titanium dioxide (TiO_{2-x}) [67]. Therefore, this structure was applied as the adsorption carrier for Pd, simulating the base configuration of the composite material. The structures of monatomic palladium, cluster palladium and nano-palladium were optimized, the three models are shown in Figs. S9a-c (Supporting information).

Figs. S9d-f (Supporting information) display differential charge density maps for the three Pd shapes. It is evident that the presence of Pd results in an accumulation of electrons on the carrier, favoring enhanced catalytic performance, consistent with experimental results. Additionally, single-atom Pd induces the highest electron transfer between the single Pd atom and the substrate [68]. Although Pd clusters and Pd nanosheets exhibit larger overall charge transfer to the substrate, the charge transfer to each atom is smaller than that for single-atom Pd. The increased electron transfer in Pd_1@TiO_{2-x} activates the reaction, thereby promoting improved HER performance.

For the HER reaction in acidic electrolyte, the Gibbs free energy of hydrogen adsorption (ΔG_{H^*}) is a crucial factor for evaluating hydrogen evolution activity. As shown in Fig. S9g (Supporting information), the ΔG_{H^*} for pure TiO_2 is −2.77 eV, indicating weak adsorption of H*. TiO_{2-x} exhibits a ΔG_{H^*} of −1.16 eV, signifying a substantial reduction in the Gibbs free energy for adsorbing active hydrogen due to the presence of oxygen vacancies. This demonstrates that the presence of oxygen vacancies significantly enhances the interaction between surface oxygen atoms and H*. After introducing metal Pd, a significant reduction in ΔG_{H^*} values is observed, indicating that Pd is the primary catalytic active site. Notably, single-atom Pd exhibits the smallest ΔG_{H^*} value, at −0.06 eV, lower than Pd clusters (−0.42 eV), Pd nanoparticles (−0.88 eV), and even commercial Pt@C (−0.09 eV). To understand the role of single-atom Pd on the carrier surface, the influence of different Pd shapes on the density of states (PDOS) distribution of d-band electrons on oxygen-deficient titanium dioxide carriers was investigated, as shown in Figs. S9h-j (Supporting information). Pd 3d orbitals, as active sites, influence the formation of the Pd-H bond, a key factor in the HER process [69]. According to the d-band center theory, the coupling of the molecular orbitals of adsorbates with the d orbitals of metal Pd can form two different orbitals: completely occupied bonding orbitals and partially occupied antibonding orbitals. According to the valence bond theory, the occupancy of electrons in antibonding orbitals determines the stability of the system to some extent, that is, the strength of the Pd-H bond. Compared to Pd nanoparticles and Pd clusters, single-atom Pd has a smaller d-band center value, indicating that single-atom Pd exhibits more occupied electronic state [70]. From the figures, it can be observed that single-atom Pd maximally promotes the shift of the d-band center away from the Fermi level, weakens the strength of the Pd-H bond, and lowers the adsorption energy of H. The d-band center of Pd nanosheets is closer to the Fermi level, indicating a stronger interaction with adsorbed H, stronger adsorption energy. This results in the difficulty of H desorption and a larger hydrogen evolution reaction energy barrier [71]. Single-atom Pd has a moderate interaction with H, leading to a d-band center that tends toward zero, making the free energy of adsorption and desorption approach zero, facilitating the progress of the HER.

This study employed an efficient hydrothermal method to synthesize oxygen-deficient titanium dioxide nanosheets (TiO_{2-x}), and subsequently anchored single-atom Pd on the carrier surface through photo-reduction deposition. Pd@TiO_{2-x}(1.5%) exhibited a low overpotential of 24 mV and a Tafel slope of 41.9 mV/dec, achieving a current density of only 10 mA/cm^2 in acidic conditions. Furthermore, the hydrogen evolution reaction (HER) performance remained stable without degradation after continuous operation for 10 h. Density functional theory (DFT) calculations indicated that single-atom Pd possessed a ΔG_{H^*} value of −0.06 eV, lower than that of Pd clusters and Pd nanoparticles. The projected density of states (PDOS) results demonstrated that single-atom Pd, by optimizing the electron density around it, forms a strong chemical interaction with the carrier, resulting in a unique electronic structure and more oxygen vacancies. This enhancement promoted the adsorption of protons and the desorption of hydrogen. The presence of oxygen vacancies provided additional active hydrogen adsorption sites, facilitating the generation of active hydrogen and optimizing the material's activity and conductivity. The synergistic effects of these factors collectively contributed to the improvement of catalytic performance.

Declaration of competing interest

The authors declare that they have no known competing financial interests or personal relationships that could have appeared to influence the work reported in this paper.

CRediT authorship contribution statement

Xiaoyu Zhao: Writing – review & editing, Writing – original draft, Supervision, Investigation, Conceptualization. **Kai Gao:** Methodology, Formal analysis, Data curation. **Sen Xue:** Visualization, Validation, Data curation. **Wei Ran:** Software. **Rui Liu:** Writing – review & editing, Project administration, Funding acquisition.

Acknowledgments

This work was financially supported by the Key Project of Tianjin Natural Science Foundation (No. 23JCZDJC00570), Special Funding of China Postdoctoral Science Foundation (No. 2023T160268), China Postdoctoral Science Foundation (No. 2023M741362), the National natural science foundation of China (Nos. 22276209 and 21822608), and Research Center for Eco-Environmental Science (No. RCEES-TDZ-2021-7). R. Liu acknowledges the support from the Youth Innovation Promotion Association of CAS (No. Y2021019).

Supplementary materials

Supplementary material associated with this article can be found, in the online version, at doi:10.1016/j.cclet.2024.110309.

References

[1] Q. Gao, W. Zhang, Z. Shi, et al., Adv. Mater. 31 (2019) 1802880.
[2] Z. He, X. Huang, Q. Chen, M. Zhu, J. Colloid Interface Sci. 616 (2022) 279–286.
[3] K. Pramoda, C.N.R. Rao, J. Mater, Chem. A 11 (2023) 16933–16962.
[4] M. Muhyuddin, G. Tseberlidis, M. Acciarri, et al., J. Energy Chem. 87 (2023) 256–285.
[5] L.N. Shi, L.T. Cui, Y.R. Ji, et al., Coord. Chem. Rev. 469 (2022) 214668.
[6] X. Zhao, X. Lu, W. Chen, et al., J. Colloid Interface Sci. 659 (2024) 11–20.

[7] J. Li, Z. Jing, H. Bai, et al., Environ. Chem. Lett. 21 (2023) 2583–2617.
[8] P. Aggarwal, D. Sarkar, K. Awasthi, P.W. Menezes, Coord. Chem. Rev. 452 (2022) 214289.
[9] C. Lei, W. Zhou, Q. Feng, et al., Nano-Micro Lett. 11 (2019) 1–10.
[10] X. Shi, C. Dai, X. Wang, et al., Nat. Commun. 13 (2022) 1287.
[11] X. Liu, Z. Hao, H. Wang, et al., Proc. Natl. Acad. Sci. U. S. A. 119 (2022) e2119723119.
[12] H. Zhao, X. Yang, Y. Duan, Z. Shen, ChemCatChem 16 (2024) e202301295.
[13] C.Z. Yuan, K.S. Hui, H. Yin, et al., ACS Mater. Lett. 3 (2021) 752–780.
[14] J. Li, J. Hu, M. Zhang, et al., Nat. Commun. 12 (2021) 3502.
[15] E. Heydari-Bafrooei, S. Askari, Int. J. Hydrog, Energy. 42 (2017) 2961–2969.
[16] Z. Pu, I.S. Amiinu, R. Cheng, et al., Nano-Micro Lett. 12 (2020) 1–29.
[17] X. Liu, S. Gao, P. Yang, et al., Appl. Mater. Today 13 (2018) 158–165.
[18] X. Wu, H. Zhang, S. Zuo, et al., Nano-Micro Lett. 13 (2021) 136.
[19] F. Zheng, C. Zhang, X. Gao, et al., Electrochim. Acta 306 (2019) 627–634.
[20] N.W.J. Scott, N.Jeddi M.J.Ford, A. Eyles, et al., J. Am. Chem. Soc. 143 (2021) 9682–9693.
[21] X. Gao, G. Yu, L. Zheng, et al., ACS Appl. Energy Mater. 2 (2019) 966–973.
[22] J. Chen, Y. Ha, R. Wang, et al., Nano-Micro Lett. 14 (2022) 186.
[23] Z. Chen, S. Yun, L. Wu, et al., Nano-Micro Lett. 15 (2023) 4.
[24] B. Geng, X. Chu, L. Liu, et al., Chin. Chem. Lett. 35 (2024) 108924.
[25] H. Yu, Y. Xue, B. Huang, et al., iScience 11 (2019) 31–41.
[26] J. Zhu, L. An, X. Li, et al., Appl. Surf. Sci. 644 (2024) 158809.
[27] B. Guo, Y. Ding, H. Huo, et al., Nano-Micro Lett. 15 (2023) 57.
[28] A.S.B. Mohd-Najib, M. Iqbal, M.B. Zakaria, et al., J. Mater. Chem. A 8 (2020) 19788–19792.
[29] X. Chen, S. Guan, J. Zhou, et al., Catalysts 62 (2023) e202312734.
[30] C. Zhai, Y. Chen, X. Huang, et al., Environ. Funct. Mater. 1 (2022) 219–229.
[31] Q. Qiao, Y. Chen, Y. Wang, et al., Chin. Chem. Lett. 34 (2023) 107394.
[32] H. Zhang, Q. Liu, Z. Shen, Chin. Chem. Lett. 35 (2024) 108607.
[33] S.H. Wang, L.N. Chen, P.Y. Zhang, et al., Nano Energy 88 (2021) 106211.
[34] X. Zeng, Y. Bai, S.M. Choi, et al., Mater. Today Nano 6 (2019) 100038.
[35] C. Li, N.C.S. Selvam, J. Fang, Nano-Micro Lett. 15 (2023) 83.
[36] X. You, D. Zhang, X.G. Zhang, et al., Nano-Micro Lett. 16 (2024) 53.
[37] J. Yang, M. Zhang, M. Chen, et al., Adv. Mater. 35 (2023) 2209885.
[38] T. Zhang, T. Yang, G. Qu, et al., J. Energy Chem. 68 (2022) 71–77.
[39] T. Zhang, T. Yang, B. Li, S. Wei, W. Gao, J. Alloys Compd. 905 (2022) 164165.
[40] Z. Wu, P. Yang, Q. Li, et al., Angew. Chem. Int. Ed. 135 (2023) e202300406.
[41] M. Zhou, X. Jiang, W. Kong, et al., Nano-Micro Lett. 15 (2023) 166.
[42] M. Song, Q. Zhang, T. Shen, et al., Chin. Chem. Lett. 35 (2024) 109083.
[43] A. Zhao, J. Masa, W. Xia, J. Energy Chem. 23 (2014) 701–707.
[44] C. Wang, Q. Zhang, B. Yan, et al., Nano-Micro Lett. 15 (2023) 52.
[45] K. He, Z. Huang, C. Chen, et al., Nano-Micro Lett. 16 (2023) 23.
[46] Z. Zeng, S. Küspert, S.E. Balaghi, et al., Small 19 (2023) 2205885.
[47] J. Zhang, M. Zhang, W. Li, et al., J. Phys. Chem. C 112 (2008) 19506–19515.
[48] W. He, X. Zhang, K. Zheng, et al., Angew. Chem. Int. Ed. 62 (2023) e202213365.
[49] N. Xu, K. Wang, Y. Zhu, Y. Zhang, Adv. Mater. 35 (2023) e2303173.
[50] W. Wu, S. Bu, L. Bai, et al., Nanoscale 15 (2023) 5909–5918.
[51] T. Luo, J. Huang, Y. Hu, et al., Adv. Funct. Mater. 33 (2023) 2213058.
[52] L. Chen, S.I. Allec, M.T. Nguyen, et al., J. Am. Chem. Soc. 145 (2023) 10847–10860.
[53] C. Wang, X. Liu, J. Wang, et al., Chin. Chem. Lett. 35 (2024) 108739.
[54] Y. Zhao, L. Tao, Chin. Chem. Lett. 35 (2024) 108571.
[55] S. Wu, X. Liu, X. Lian, et al., Adv. Mater. 30 (2018) 1802173.
[56] S. Wang, T. Ding, T. Liu, et al., Angew. Chem. Int. Ed. 62 (2023) e202218630.
[57] E.D. Corro, M. Taravillo, V.G. Baonza, Phys. Rev. B 85 (2012) 033407.
[58] S. Wan, Y. Chen, S. Fang, et al., Nat. Mater. 20 (2021) 624–631.
[59] K.M. Naik, E. Higuchi, H. Inoue, Nanoscale 12 (2020) 11055–11062.
[60] M. Zhang, W. Guo, Y. Chen, et al., Chin. Chem. Lett. 34 (2023) 108229.
[61] H. Wei, X. Li, B. Deng, et al., Chin. J. Catal. 43 (2022) 1058–1065.
[62] J.Y. Yue, X.L. Ding, L.P. Song, et al., Micropor. Mesopor. Mat. 5 (2021) 3859–3866.
[63] F. Meng, X. Qin, L. Yang, et al., Small 18 (2022) 2203283.
[64] Z. Wei, H. Wang, C. Zhang, et al., Angew. Chem. Int. Ed. 60 (2021) 16622–16627.
[65] Y. Chen, L. Soler, M. Armengol-Profitós, et al., Appl. Catal. B 309 (2022) 121275.
[66] W. He, X. Zhang, K. Zheng, et al., Angew. Chem. Int. Ed. 62 (2023) e202213365.
[67] J. Cui, Z. Hao, Y. Wang, et al., Chem. Eng. J. 446 (2022) 136989.
[68] O.A. Qamar, F. Jamil, M. Hussain, et al., Chem. Eng. J. 460 (2023) 141734.
[69] X. Chen, M. Peng, X. Cai, et al., Nat. Commun. 12 (2021) 2664.
[70] S. Ji, Y. Chen, G. Zhao, et al., Appl. Catal. B 304 (2022) 120922.
[71] S. Weon, M.J Suh, C. Chu, et al., Environ. Sci. Technol. 1 (2021) 512–522.